Evaluation of the Simulated Interannual and Subseasonal Variability in an AMIP-Style Simulation Using the CSU Multiscale Modeling Framework

MARAT KHAIROUTDINOV,* CHARLOTTE DEMOTT, AND DAVID RANDALL

Department of Atmospheric Science, Colorado State University, Fort Collins, Colorado

ABSTRACT

The Colorado State University (CSU) Multiscale Modeling Framework (MMF) is a new type of general circulation model (GCM) that replaces the conventional parameterizations of convection, clouds, and boundary layer with a cloud-resolving model (CRM) embedded into each grid column. The MMF has been used to perform a 19-yr-long Atmospheric Model Intercomparison Project–style simulation using the 1985–2004 sea surface temperature (SST) and sea ice distributions as prescribed boundary conditions. Particular focus has been given to the simulation of the interannual and subseasonal variability.

The annual mean climatology is generally well simulated. Prominent biases include excessive precipitation associated with the Indian and Asian monsoon seasons, precipitation deficits west of the Maritime Continent and over Amazonia, shortwave cloud effect biases west of the subtropical continents due to insufficient stratocumulus clouds, and longwave cloud effect biases due to overestimation of high cloud amounts, especially in the tropics. The geographical pattern of the seasonal cycle of precipitation is well reproduced, although the seasonal variance is considerably overestimated mostly because of the excessive monsoon precipitation mentioned above. The MMF does a good job of reproducing the interannual variability in terms of the spatial structure and magnitude of major anomalies associated with El Niño–Southern Oscillation (ENSO).

The subseasonal variability of tropical climate associated with the Madden–Julian oscillation (MJO) and equatorially trapped waves are particular strengths of the simulation. The wavenumber–frequency power spectra of the simulated outgoing longwave radiation (OLR), precipitation rate, and zonal wind at 200 and 850 mb for time scales in the range of 2–96 days compare very well to the spectra derived from observations, and show a robust MJO and Kelvin and Rossby waves with phase speeds similar to those observed. The geographical patterns of the MJO and Kelvin wave–filtered OLR variance for summer and winter seasons are well simulated; however, the variances tend to be overestimated by as much as 50%. The observed seasonal and interannual variations of the strength of the MJO are also well reproduced.

The physical realism of the simulated marine stratocumulus clouds is demonstrated by an analysis of the composite diurnal cycle of cloud water content, longwave (IR) cooling, vertical velocity variance, rainfall, and subcloud vertical velocity skewness. The relationships between vertical velocity variance, IR cooling, and negative skewness all suggest that, despite the coarse numerical grid of the CRM, the simulated clouds behave in a manner consistent with the understanding of the stratocumulus dynamics. In the stratocumulus-to-cumulus transition zone, the diurnal cycle of the inversion layer as simulated by the MMF also bears a remarkable resemblance to in situ observations. It is demonstrated that in spite of the coarse spacing of the CRM grid used in the current version of MMF, the bulk of vertical transport of water in the MMF is carried out by the circulations explicitly represented on the CRM grid rather than by the CRM's subgrid-scale parameterization.

1. Introduction

In a new type of general circulation model (GCM), many processes that are unresolved on the GCM's grid

* Current affiliation: School of Marine and Atmospheric Sciences, Stony Brook University, Stony Brook, New York.

Corresponding author address: Marat Khairoutdinov, School of Marine and Atmospheric Sciences, Stony Brook University, Stony Brook, NY 11795-5000.
E-mail: mkhairoutdin@ms.cc.sunysb.edu

are incorporated using a cloud-resolving model (CRM; Grabowski and Smolarkiewicz 1999; Grabowski 2001; Khairoutdinov and Randall 2001; Khairoutdinov et al. 2005, hereafter K05). The CRM, which in this context is often called a superparameterization, is inserted into each GCM grid column. From the GCM's perspective, the CRM works like a set of conventional parameterizations. The CRM is forced by the GCM grid-scale tendencies, and the CRM generates vertical profiles of such tendencies. Such a superparameterized GCM has been termed a multiscale modeling framework (MMF).

This name emphasizes that such a model includes in a single framework not only the scales of atmospheric motion on the order of hundreds of kilometers, as represented on the GCM's grid, but also the mesoscale and cloud-scale circulations that are represented on the CRM's grid. In this sense, MMF is regarded as a bridge between the conventional GCMs and the immensely more computationally expensive global CRMs that have just recently been applied for short global simulations (Tomita et al. 2005; Miura et al. 2005).

A major strength of the MMF concept is that it allows cloud microphysics, aerosols, turbulence, and radiation to interact on the *cloud* scale, as they do in nature. In contrast, various parameterizations of unresolved physical processes in conventional GCMs do not typically communicate directly with each other, but rather through modification of the scales that are represented on the GCM's coarse grid, which are generally much larger than the cloud scale. Recent experiments with the MMF have indicated that such cloud-scale interactions ignored in conventional GCMs can be quite important. For example, K05 have shown that the MMF tends to improve the diurnal cycle of precipitation over summertime continents quite dramatically when compared to the conventional version of the same GCM. Cole et al. (2005) have demonstrated the importance of cloud-scale interactions between clouds and radiation for the simulated global distribution of clouds and radiation. The problem of the scale of interactions represents just one of many problems associated with the current state of the art of the physical parameterizations, and the MMF approach is argued to be one of the plausible pathways to the future (Randall et al. 2003; Arakawa 2004).

The MMF has a substantially higher computational cost than a conventional GCM. For example, when run on the same number of central processing units (CPUs) in our first MMF experiment (Khairoutdinov and Randall 2001), the Colorado State University (CSU) MMF was about two orders of magnitude slower than the host GCM with conventional parameterizations. However, because the ratio of the time that the MMF spent computing to the time spent for inter-CPU communication is much higher than the same ratio for conventional GCMs, the MMF can be vastly more scalable on parallel computers; that is, it can utilize a large number of CPUs more efficiently than conventional GCMs. For example, the CSU MMF results presented in this paper were obtained using 1024 CPUs of the "Seaborg" supercomputer at the Department of Energy's National Energy Research Scientific Computing Center (NERSC), with more than 90% parallel efficiency (see Fig. 2 of K05).

It is expected that over the next decade, the computational performance of the CSU MMF will improve further on the faster systems of the future, so that century-long climate-change simulations using a coupled atmosphere–ocean MMF model may become feasible. Even now, it is feasible to make runs as long as a decade. For example, the CSU MMF was recently used to conduct a relatively simple Cess-type climate sensitivity experiment (Cess et al. 1996). The results were reported by Wyant et al. (2006). A multiyear control simulation was compared to an experiment in which the prescribed climatological sea surface temperature (SST) was uniformly increased by 2 K.

It has also become feasible to use the MMF in Atmospheric Model Intercomparison Project (AMIP)–style simulations based on prescribed observed monthly mean SSTs and sea ice cover, for a period of more than a decade. Recently, short AMIP-style MMF simulations using the 1998–99 observed SSTs were conducted at the Pacific Northwest National Laboratory (Ovtchinnikov et al. 2006) with a version of MMF similar to the CSU MMF, and also at the National Aeronautics and Space Administration (NASA) Goddard Space Flight Center (Tao et al. 2007, manuscript submitted to *Bull. Amer. Meteor. Soc.*) using a completely different MMF.

In this paper, we present the results of the first AMIP-style simulation with the CSU MMF using the 1985–2004 observed SSTs. The emphasis of our analysis is on the simulated subseasonal and interannual variability as compared to that in the observations.

2. Simulation setup

The CSU MMF was described in detail by K05. The host GCM is the National Center for Atmospheric Research (NCAR) Community Atmosphere Model (CAM), version 3, which is the atmospheric component of the NCAR Community Climate System Model (Collins et al. 2006). We use a semi-Lagrangian dynamical core because it allows us to achieve better scalability of the MMF when using a large number of processors. The dynamical core was configured to run with $2.8° \times 2.8°$ horizontal grid spacing (T42 truncation) with 30 levels, and the domain top was at 3.6 hPa. The GCM time step was 30 min. In each grid column, all of the conventional moist physics, convective, turbulence, and boundary layer parameterizations, except for the gravity wave drag parameterization, were replaced by a CRM, which is a two-dimensional version of the System for Atmospheric Modeling (SAM; Khairoutdinov and Randall 2003).

The CRM solves the momentum equations using the anelastic approximation. The prognostic thermody-

TABLE 1. Global annual mean climatological properties of CSU MMF vs observational estimates.

Property	MMF	CAM	Obs	Source
TOA outgoing longwave radiation (W m^{-2})	238.3	234.6	234.1	ISCCP-FD
TOA absorbed solar radiation (W m^{-2})	237.6	236.8	238.3	ISCCP-FD
Longwave cloud forcing (W m^{-2})	24.5	29.6	25.6	ISCCP-FD
Shortwave cloud forcing (W m^{-2})	-52.5	-54.9	-50.0	ISCCP-FD
Net surface longwave radiation (W m^{-2})	56.2	56.4	49.4	ISCCP-FD
Clear-sky net surface longwave radiation (W m^{-2})	83.7	86.1	78.7	ISCCP-FD
Net surface shortwave radiation (W m^{-2})	158.8	158.8	165.9	ISCCP-FD
Clear-sky surface shortwave radiation (W m^{-2})	216.4	218.5	218.6	ISCCP-FD
Precipitation rate (mm day^{-1})	2.80	2.83	2.66	CMAP
Cloud water path (mm)	0.093	0.129	0.122	MODIS**
Precipitable water (mm)	25.1	24.4	24.6	NVAP
Latent heat flux (W m^{-2})	81.2	81.9	78.0	KT97
Sensible heat flux (W m^{-2})	22.9	19.7	24.0	KT97
Total cloud amount (%)	67.0*	62.6*	66.9	ISCCP
Low cloud amount (%)	25.8*	21.0*	26.4	ISCCP
Middle cloud amount (%)	13.0*	10.0*	19.1	ISCCP
High cloud amount (%)	28.2*	31.6*	21.3	ISCCP

* ISCCP simulator (Klein and Jacob 1999).
** Moderate Resolution Imaging Spectroradiometer (King et al. 2003).

namic variables include the liquid/ice water moist static energy, total precipitating, and total nonprecipitating water. Cloud condensate is diagnosed using the "all or nothing" condensation scheme, assuming saturation with respect to water/ice. Precipitating water is a mixture of the snow, graupel, and rainwater with the hydrometeor partitioning assumed to be a function of temperature only. The precipitation sources and sinks are computed using a simple bulk microphysics model.

In this study, the CRM's two-dimensional domain had 32 grid columns with 4-km horizontal grid spacing, and 28 layers collocated with the GCM grid layers. The time step was 20 s. The domain was periodic and aligned in the south–north direction; this is different from K05, who used the east–west alignment. The motivation for this change is that it seems to mitigate the positive precipitation bias in the western Pacific for the summer months (K05). The physical reason for the improvement is not yet clear and is a subject of current research.

The subgrid-scale (SGS) fluxes were computed using the first-order turbulent closure based on the Smagorinski model (Smagorinski 1963) for the eddy diffusivity and viscosity. The CAM radiative transfer scheme was applied every 15 min for each CRM column using the all-or-nothing cloud overlap assumption.

During the GCM time step, the CRM was forced by the large-scale tendencies arising from GCM dynamical processes. The forcing was applied uniformly in the horizontal, and computed as described in K05. The CRM output consisted of horizontally averaged tendencies of temperature, water vapor, and cloud conden-

sate, which were used to feed back on the GCM fields. The GCM's horizontal wind was not modified by the CRM because of concern that the vertical momentum transport simulated by the two-dimensional model is unrealistic. Instead, the conventional parameterizations of the host GCM were allowed to alter the wind field (see the discussion and experiments reported by K05). The surface fluxes were computed on the GCM grid with a local gustiness enhancement of the surface stress on the CRM grid, that is, the local surface stress perturbations were assumed to be proportional to the deviations of the near-surface velocity components from their domain-averaged values, so that the domain mean stress was not affected; in the future, all surface fluxes will be computed on the CRM grid.

The AMIP-style integration presented in this study was performed using prescribed monthly mean SST and sea ice. The integration period was from 1 September 1985 to 1 September 2004, that is, a total of 19 yr was simulated. The monthly and yearly means were computed for 1986 through 2003.

3. Results

a. Simulated annual mean climatology

In this section, the main results of the mean annual climatology are presented. The MMF results are compared with the standard CAM (version 3; T42 spatial truncation) annual climatology. Note that the CAM annual climatology, including the CAM column in Table 1, is included in this paper only as a reference, and will
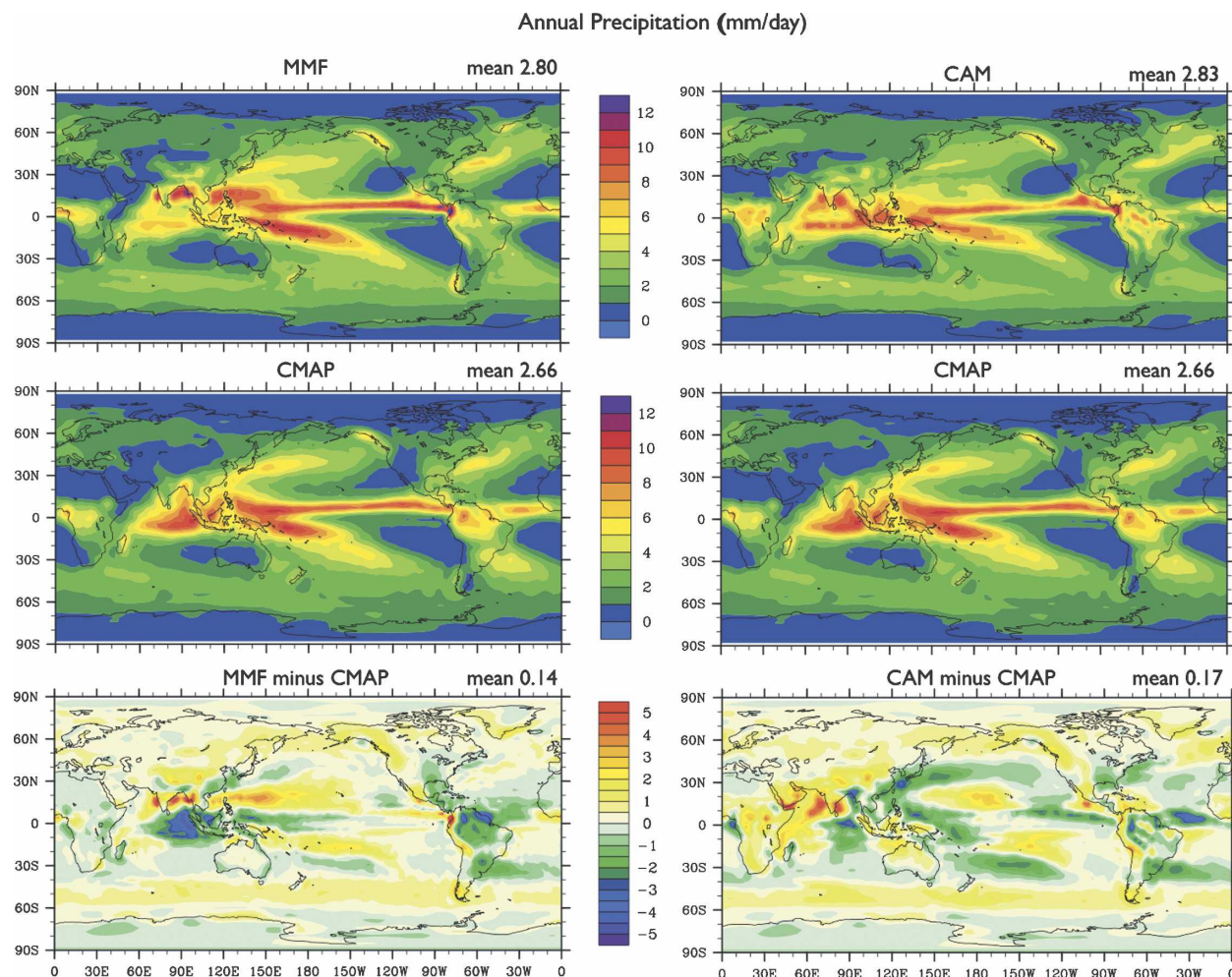
Annual Precipitation (mm/day)

FIG. 1. Annual mean precipitation (mm day^{-1}) for (top left) MMF, (top right) CAM, (middle) CMAP observations, and (bottom) models minus CMAP.

not be discussed in detail. The details of the CAM simulations are discussed by Collins et al. (2006), Hack et al. (2006), and Boville et al. (2006).

The global distribution of the annual mean precipitation is shown in Fig. 1, along with the observed Climate Prediction Center (CPC) Merged Analysis of Precipitation (CMAP) climatology (Xie and Arkin 1997) and the corresponding mean difference. The overall pattern of precipitation is generally well reproduced, but there are important deficiencies. The most prominent are the deficits of precipitation in the Indian Ocean just to the west of the Maritime Continent, in the western Pacific intertropical convergence zone (ITCZ), in the South Atlantic storm track, and over Amazonia. The most notable regions of excessive simulated precipitation are the northwest tropical Pacific during the South Asian monsoon season, and western India and the Bay of Bengal during the Indian monsoon season.

Also, there is a "bull's-eye" of excessive precipitation in equatorial South America. The positive monsoon season biases have also been evident in earlier MMF simulations with prescribed climatological SSTs (K05).

There is a clear underestimation of precipitation in the region where the ITCZ and the South Pacific convergence zone merge, and an overestimation just south of the equator, a manifestation of the double-ITCZ problem. Precipitation in Africa and Eurasia is generally well simulated, while considerable biases are present in North and South America. The global mean annual precipitation is overestimated by about 0.14 mm day^{-1} with respect to the CMAP estimate of 2.66 mm day^{-1} (Table 1).

The geographical distribution of the annually averaged column-integrated water vapor, or precipitable water, and its difference from the NASA Water Vapor Project (NVAP; Randel et al. 1996) climatology, is
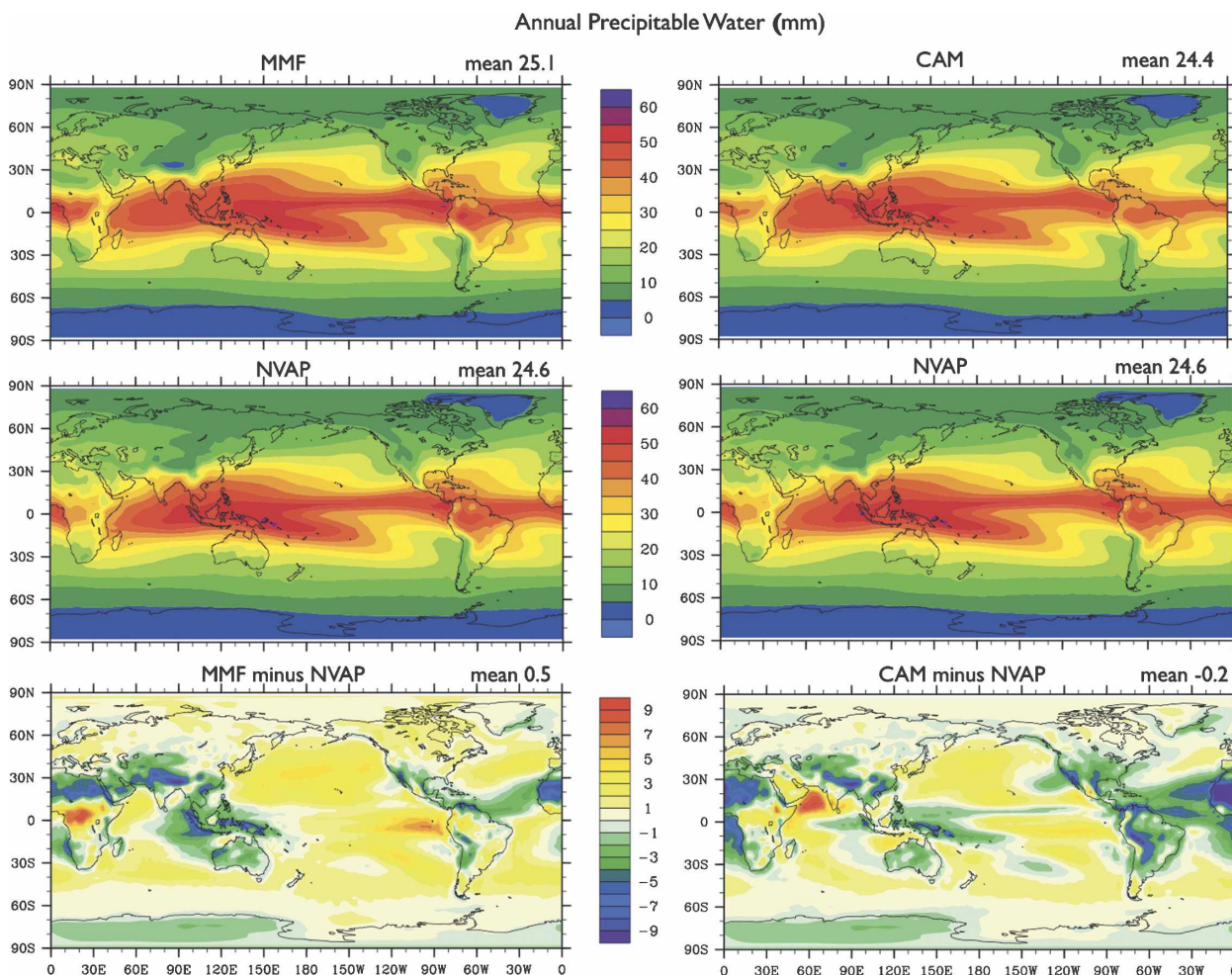
Annual Precipitable Water (mm)

FIG. 2. Annual mean precipitable water (mm) for (top left) MMF, (top right) CAM, (middle) NVAP observations, and (bottom) models minus NVAP.

shown in Fig. 2. Although the MMF captures the observed patterns quite well, there are considerable biases. Precipitable water is systematically overestimated over most of the oceans, with the most prominent error in the equatorial eastern Pacific. The most notable maritime negative biases are in and around the Maritime Continent and equatorial Atlantic. Over land, the simulation is systematically too dry over the subtropical continents, and too wet over central Africa, suggesting that the simulated Hadley circulation is stronger than that in nature. There is a clear tendency for unrealistically dry air over the maritime regions west of the subtropical continents, where stratocumulus clouds are observed to form. This contributes to an underestimation of low-level clouds in those regions. The globally averaged precipitable water is overestimated by about 0.5 mm (Table 1).

The global distributions of the annual mean longwave cloud effect (LWCE) and shortwave cloud effect (SWCE) are shown in Figs. 3 and 4, respectively, along with the observational estimates from the International Satellite Cloud Climatology Project (ISCCP)-Flux Data (FD) dataset (Zhang et al. 2004) and the mean error distribution for 1986–2000. The cloud effect is the difference between the clear sky and total fluxes at the top of the atmosphere (TOA), and, thus, is a direct measure of the cloud effect on the TOA radiation. The global annual mean values for MMF match the observational estimates rather well (Table 1). The effective radius of liquid water drops assumed for the shortwave radiation computations was reduced (by about 2 μm) relative to its value in the standard CAM to produce a near-zero global annual mean TOA; however, the global mean SWCE and LWCE have not been intentionally tuned. Their good match with observational estimates appears to be, however, a result of the cancellation of the rather large regional biases. The geographical distribution of LWCE biases generally re-
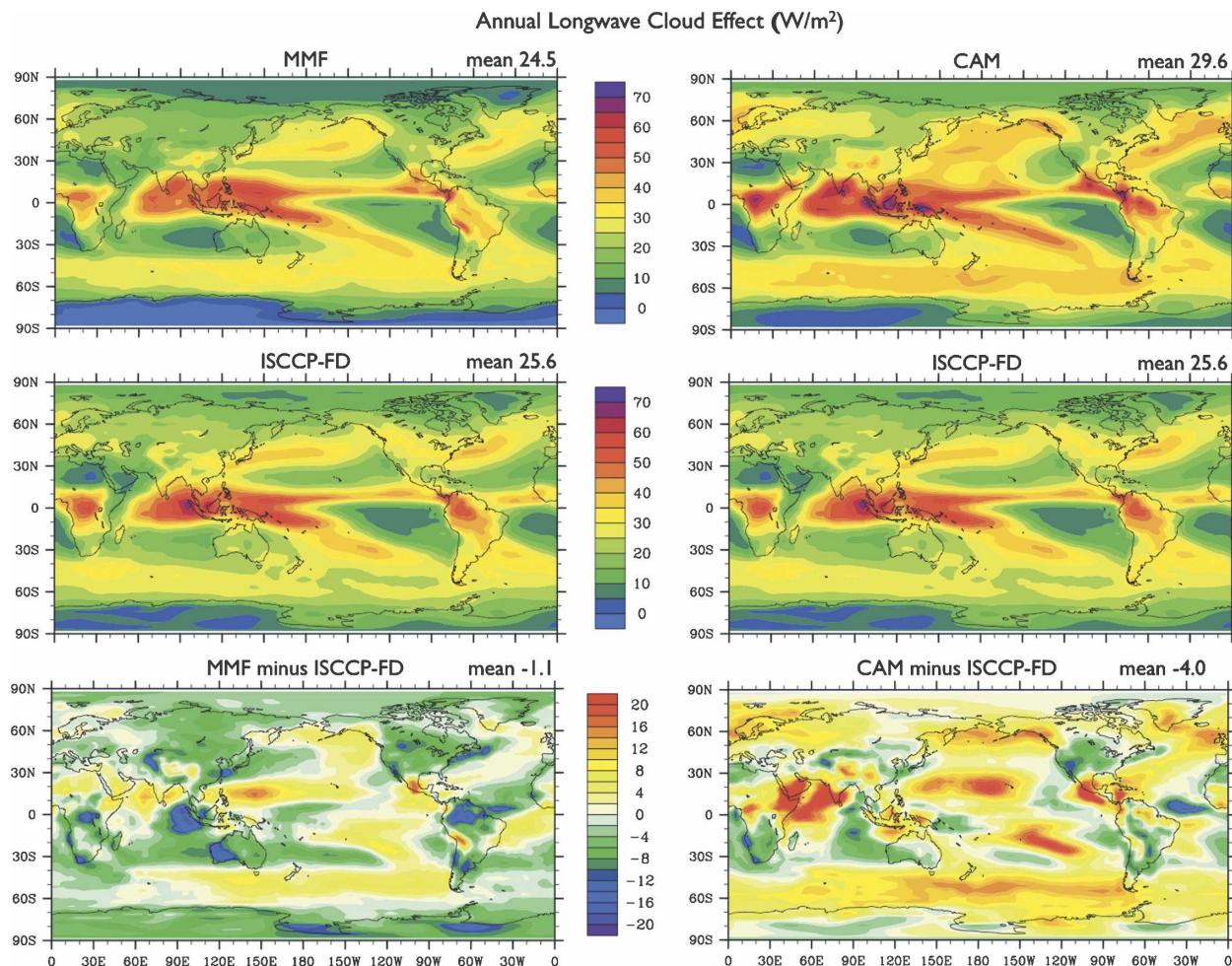
Annual Longwave Cloud Effect (W/m²)

FIG. 3. Annual mean longwave cloud effect (W m^{-2}) for (top left) MMF, (top right) CAM, (middle) ISCCP-FD observational estimates, and (bottom) models minus ISCCP-FD.

sembles the precipitation biases, which is expected since the outgoing longwave radiation is mostly affected by deep precipitating clouds. Therefore, we expect that improvements in the global distribution of precipitation will lead to a general improvement in the geographical pattern of longwave radiation.

The large negative biases in the SWCE (Fig. 4) are also well correlated with the positive precipitation biases due to the fact that there is more active deep convection and, as a result, more extensive anvils in the model that tend to reflect more sunlight back to space. The largest positive SWCE biases are, not surprisingly, situated west of the subtropical continents, where the stratocumulus clouds are mostly located. The aforementioned cloudiness biases can clearly be seen on the geographical distribution of the simulated total cloud cover (Fig. 5) in comparison with the observations. The MMF seems to overestimate the high-cloud amount in the tropics and to underestimates the occurrence of

low-level clouds, such as trade cumuli and stratocumuli. The underestimate of low-level clouds may result from either the overactive Hadley circulation, incorrect advection of atmospheric moisture into the region, or simply the inability of the cloud-resolving model to produce a realistic amount of low-level clouds because of inadequate CRM grid spacing. Further discussion is given by K05.

The net shortwave radiation absorbed by the surface is underestimated by about 7 W m^{-2} compared to the ISCCP-FD estimates (Table 1), with a much smaller bias under clear skies. Net surface longwave flux is overestimated also by 7 W m^{-2}, with a comparable bias under clear skies. Despite the biases in the surface radiation budget, the global mean turbulent surface fluxes are within 3 W m^{-2} of the Kiehl and Trenberth (1997, hereafter KT97) estimates; however, the estimates themselves are subject to significant uncertainties. The MMF simulation has biases in the zonal struc-
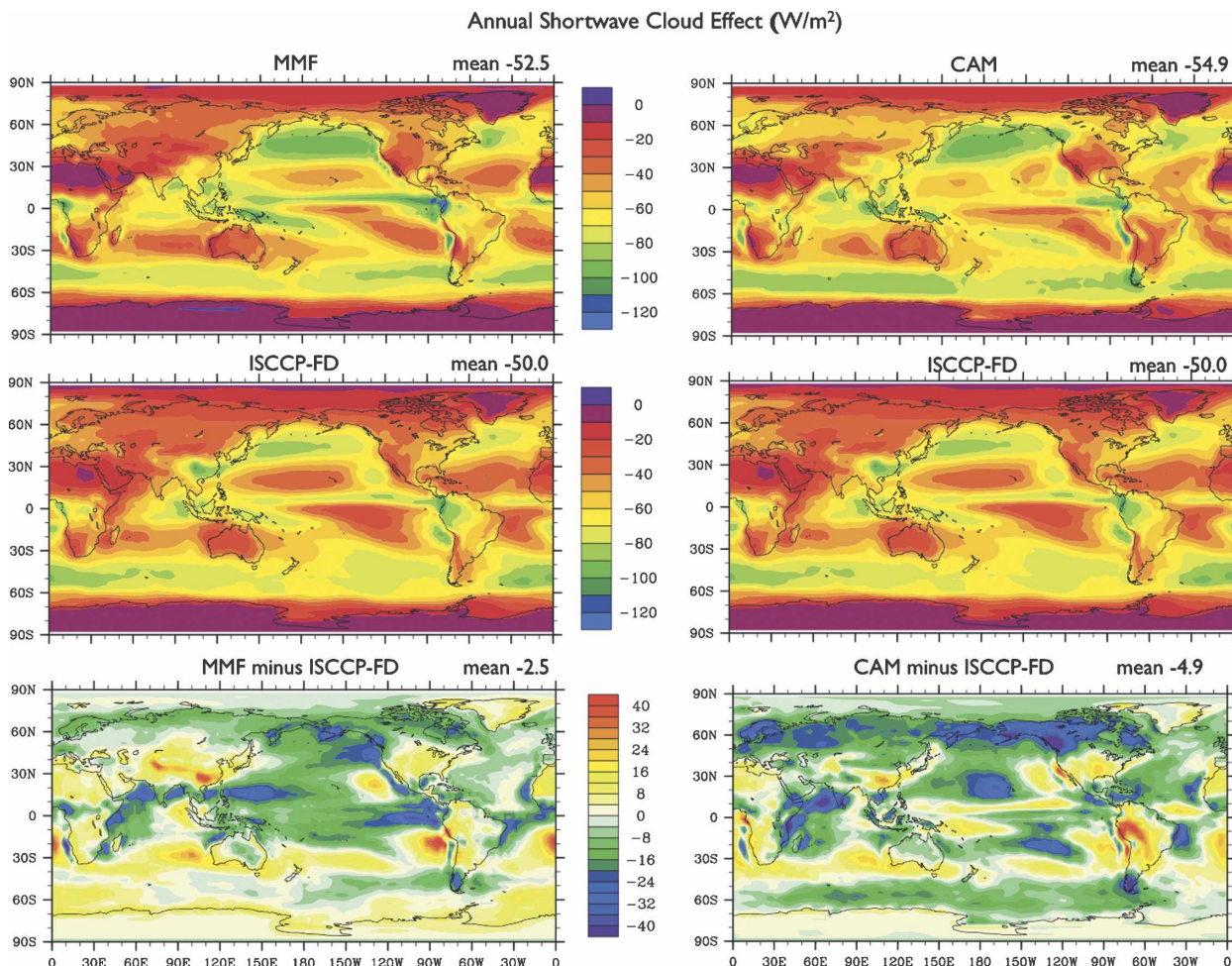
Annual Shortwave Cloud Effect (W/m²)

FIG. 4. Annual mean shortwave cloud effect (W m^{-2}) for (top left) MMF, (top right) CAM, (middle) ISCCP-FD observational estimates, and (bottom) models minus ISCCP-FD.

ture of the temperature field (not shown), which are similar to those seen in the earlier climatological SST run (see Fig. 12 of K05), with a significant cold bias in the temperature of the tropical tropopause.

b. Seasonal variability

The seasonal cycle is a major forced mode of climate variability. One of many ways to evaluate the simulated mean seasonal cycle is to look at the geographical distribution of the amplitude and phase of the first annual harmonic for various variables. Figure 6 shows the first annual harmonic of the precipitation rate, from both the MMF simulation and CMAP. The monthly mean precipitation for the period of 1986–2003 was used to define a mean annual cycle. In general, the simulated and observed patterns of the seasonal variation amplitude are quite similar. The most notable overestimation of the seasonal precipitation amplitude is in the Indian

and Asian monsoon regions, which is consistent with the large biases of the mean precipitation there (see Fig. 1). The geographical pattern of the average month of the precipitation maximum as seen in the first annual harmonic closely resembles the observed pattern. There are biases in North America and Europe, where the simulated phase is about 2 months ahead of the observations.

In the CMAP monthly data, the first annual harmonic of the precipitation rate explains 41% and 34% of the total precipitation variance in the tropics and midlatitudes,[1] respectively. The corresponding values from the MMF are 33% and 27%, respectively. These underestimates are mostly due to *overestimates* of the

---

[1] Here the tropics are defined as the belt from 30°S to 30°N, and the midlatitudes are between 30° and 60° in both hemispheres. The contribution of each grid cell was weighted by its surface area.
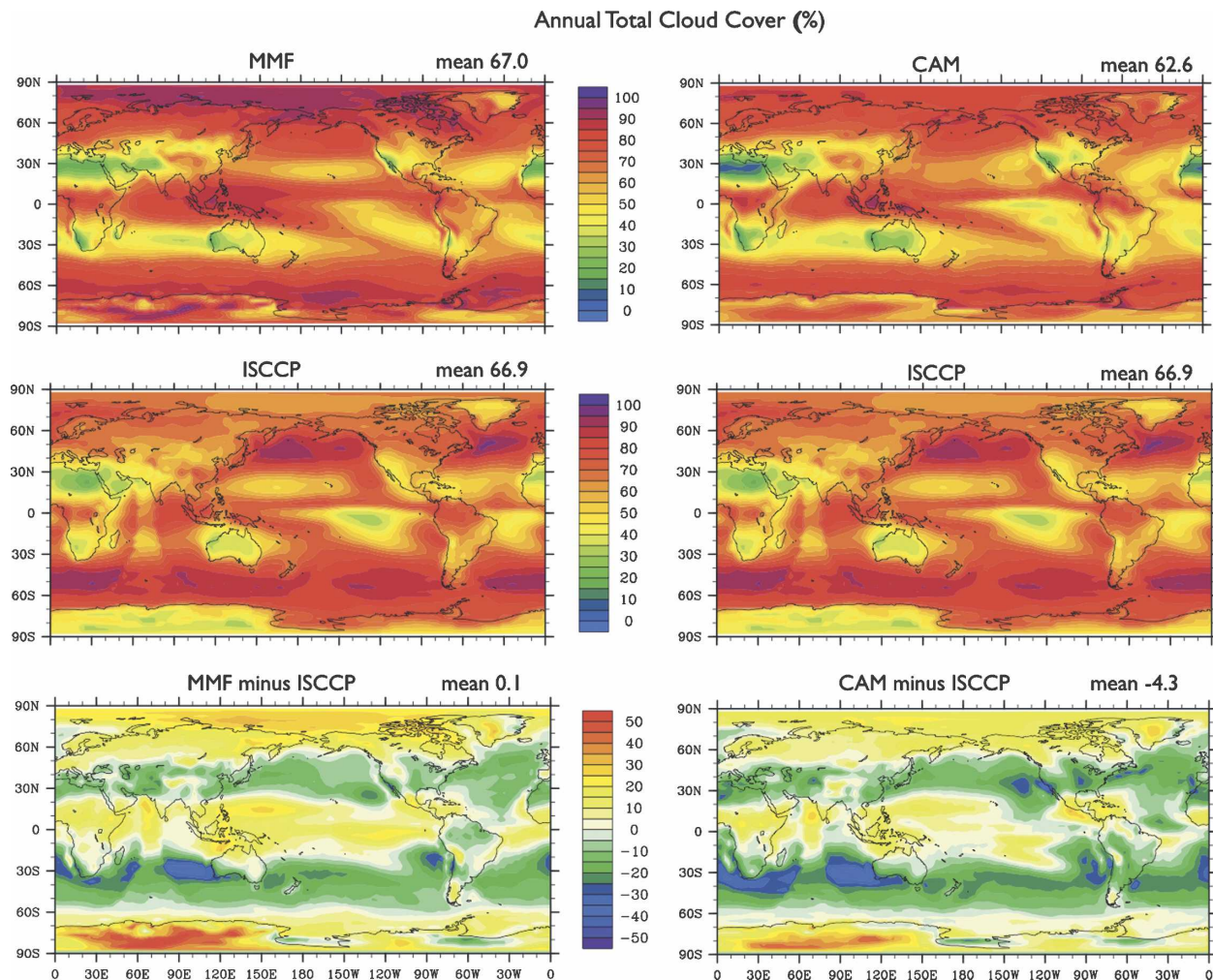
Annual Total Cloud Cover (%)

FIG. 5. Annual mean total cloud cover (%) for (top left) MMF, (top right) CAM, (middle) ISCCP observational estimates, and (bottom) models minus ISCCP. Note that the cloud cover estimates for both models were obtained using the ISCCP simulator software (Klein and Jacob 1999).

total variance of monthly precipitation for the whole AMIP run (by a factor of 1.83 for the tropics and 1.57 for midlatitudes). The ratios of the simulated to observed annual harmonic's variance in the tropics and midlatitudes, are 1.48 and 1.24, respectively, with most of the overestimation of variability of precipitation in tropics being due to an unrealistically strong annual cycle associated with the Indian and Asian monsoon biases.

c. Interannual variability

El Niño–Southern Oscillation (ENSO) is the most important mode of interannual variability on subdecadal scales, especially in the tropics. In this study of uncoupled integrations, only the forced atmospheric response to evolving but prescribed SST anomalies can be examined and compared to observations. The following two analysis methods have been used: empirical orthogonal function (EOF) analysis and simple compositing. To reveal the structure of the interannual variations, EOF analysis was applied to the bandpass-filtered monthly data, that is, the annual cycle and shorter time scales were removed by performing Fourier analysis, zeroing out the annual and shorter harmonics, and then performing Fourier synthesis. In Fig. 7, the results for the precipitation rate anomalies are compared to observations for the first and second EOFs (EOF1 and EOF2, respectively). The MMF simulation does a very good job in reproducing the spatial patterns of both modes. The simulated EOF1 explains 19% of the variance, with EOF2 explaining about half of that. This is similar to what is observed,

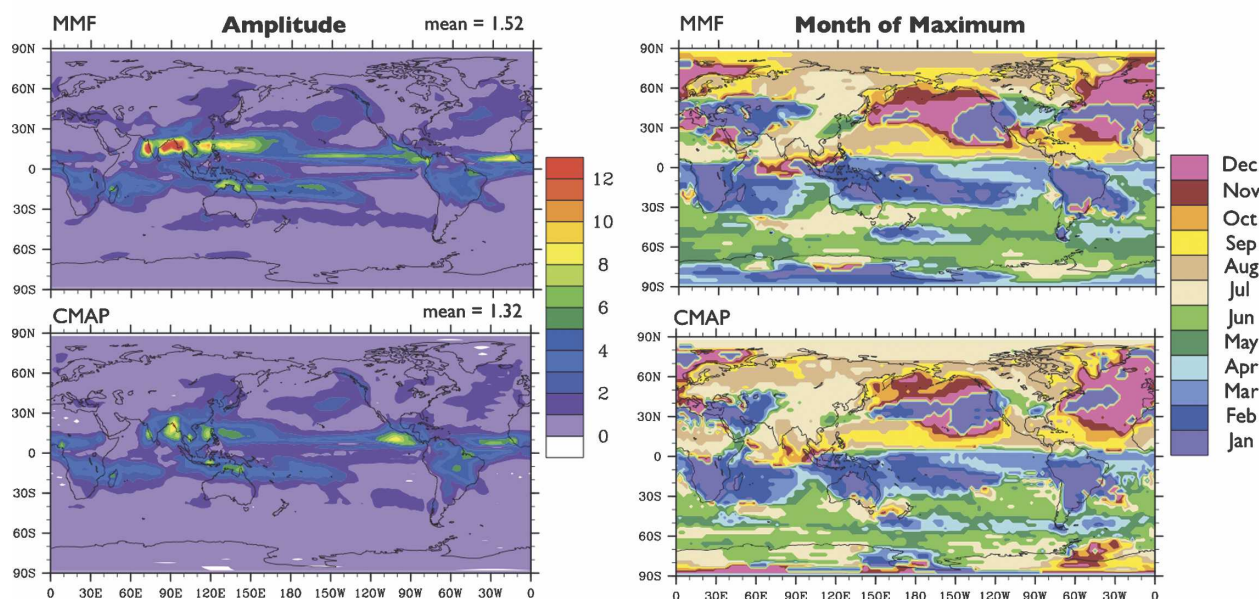## Precipitation Annual Harmonic

FIG. 6. The mean seasonal cycle of precipitation during 1986–2004 in terms of the average amplitude of the annual harmonic (top left) simulated by the MMF and (bottom left) derived from the CMAP observations. The (top right) simulated and (bottom right) observed month of maximum (phase) of the precipitation annual harmonic are shown.

except that in observations EOF1 explains up to one-third of the variance. The observed time series of principle components (PCs) of the two modes are well reproduced by the MMF, especially for the leading mode. The peaks of the PC1 time series correspond to the El Niño events, while the troughs mark the La Niña events.

Another simple way of looking at the response of the atmosphere to the ENSO SST anomalies is to look at the spatial pattern of the differences between the annually averaged anomalies for both a composite El Niño year and a composite La Niña year. The contributing years have been selected based on the observed PC1 for the precipitation rate, and the number of years for a given field was limited by the availability of observational estimates for a given ENSO phase. The same years were used for the MMF results and observations. Figure 8 shows the composite anomalies for several fields. As was the case with the precipitation anomaly, the MMF does a good job of reproducing the spatial structure and shape as well as the magnitude of major positive and negative anomalies. There are some discrepancies with respect to observations for the weaker anomalies, especially over the continents; however, the statistical significance of those differences is hard to access without running a multimember ensemble of MMF simulations, which is not currently practical. Finally, we note that the standard CAM generally reproduces the observed El Niño–La Niña pre-

cipitation and longwave cloud forcing anomalies rather well; however, the shortwave cloud forcing anomaly is significantly underestimated (not shown).

d. Subseasonal variability in the tropics

While the variability of the simulated atmosphere associated with the ENSO in the AMIP-style simulation is essentially forced by the imposed SST anomalies, the subseasonal variability for time scales of 100 days or shorter is mostly due to internal modes. Here we examine the ability of the MMF to simulate the tropical subseasonal variability associated with convectively coupled equatorial waves, such as Kelvin and equatorial Rossby waves, as well as, of course, the Madden–Julian oscillation (MJO; Madden and Julian 1972). The MJO is a major mode of subseasonal variability in the tropics and is equally important for both climate and weather prediction. MJO has teleconnections with the extratropics and is believed to play an important role in triggering El Niño events. Unfortunately, subseasonal variability, especially the MJO, is generally very poorly simulated by most contemporary GCMs (e.g., Lin et al. 2006).

In our earlier experiments with climatological SSTs (Randall et al. 2003; K05), the MMF simulations showed a robust MJO with a realistic structure. Although quite encouraging, those early experiments were relatively short—each about a year and a half—
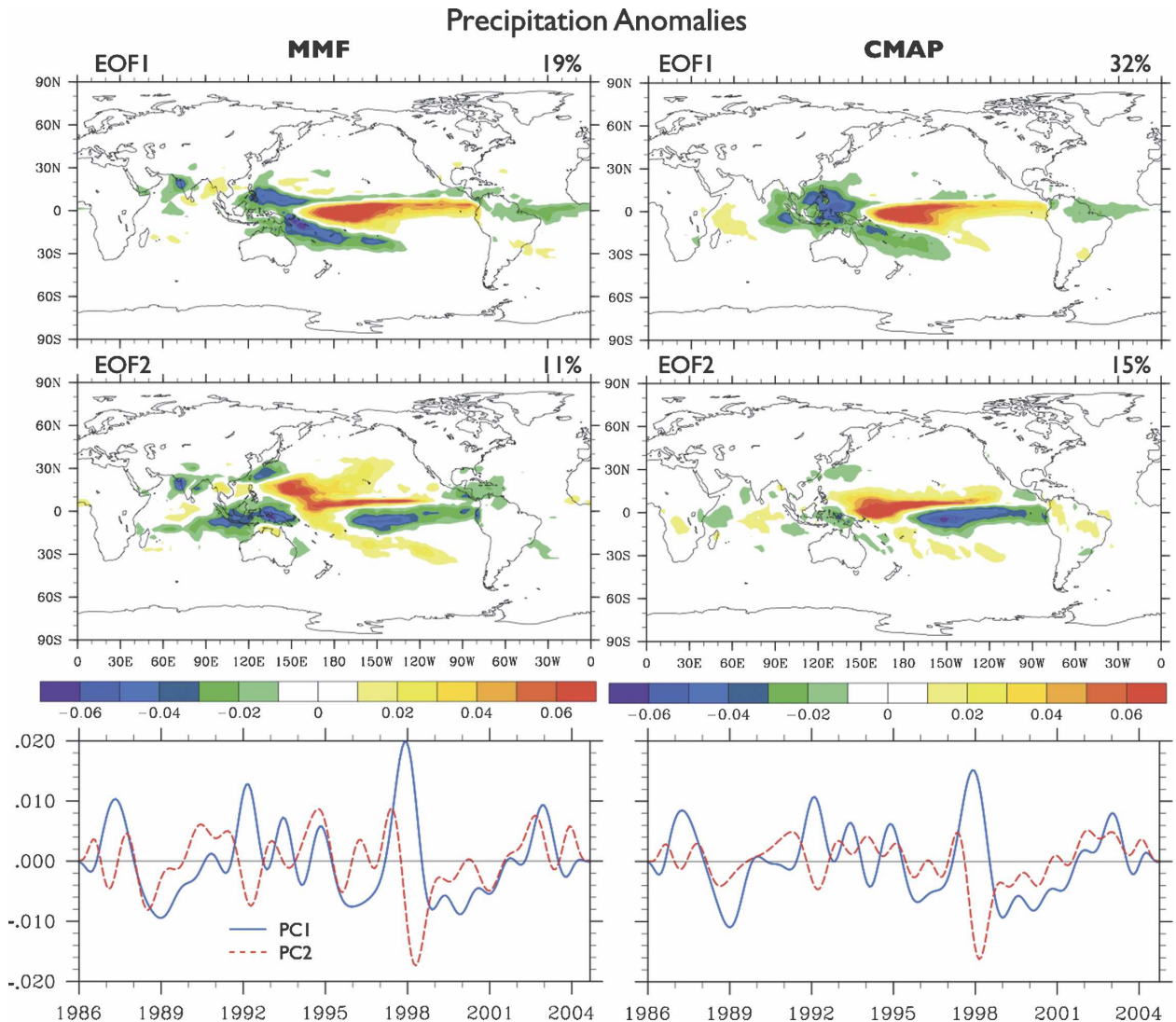
Precipitation Anomalies

FIG. 7. (top) EOF1 and (middle) EOF2 and (bottom) the associated principle component time series of bandpass-filtered monthly (left) simulated and (right) observed CMAP precipitation for years 1986–2004.

with just a few MJO events. In this study, we compared the MJO statistics as simulated by the MMF over 18-yr period with statistics derived from the similarly lengthy observations. The longer records make the comparison more robust.

It has become rather standard to look at the dominant subseasonal modes of variability using the methods of Wheeler and Kiladis (1999, hereafter WK99), who analyzed the wavenumber–frequency spectrum using the ratio of the raw spectral power to the power of a "background spectrum," which is simply a sufficiently smoothed raw spectrum. The WK99 procedure was applied to daily mean data from both the MMF and observations. To reduce the noise, the data were divided into 96-day-long segments overlapping each other by 60

days. Thus, the lowest resolved frequency was 1/96 cycle per day, while the highest frequency was 1/2 cycle per day. We looked only at the equatorially trapped waves, so only the data in the 15°S–15°N latitudinal belt were considered. For each analyzed field, two sets of wavenumber–frequency spectra were calculated—one for the symmetric and one for the antisymmetric components about the equator. Here we present the symmetric spectra only because they contain most of the power.

The wavenumber–frequency spectra for the outgoing longwave radiation (OLR) and precipitation rate as observed and from the MMF and standard CAM AMIP-style runs are shown in Fig. 9. Positive zonal wavenumbers indicate eastward-propagating disturbances; the

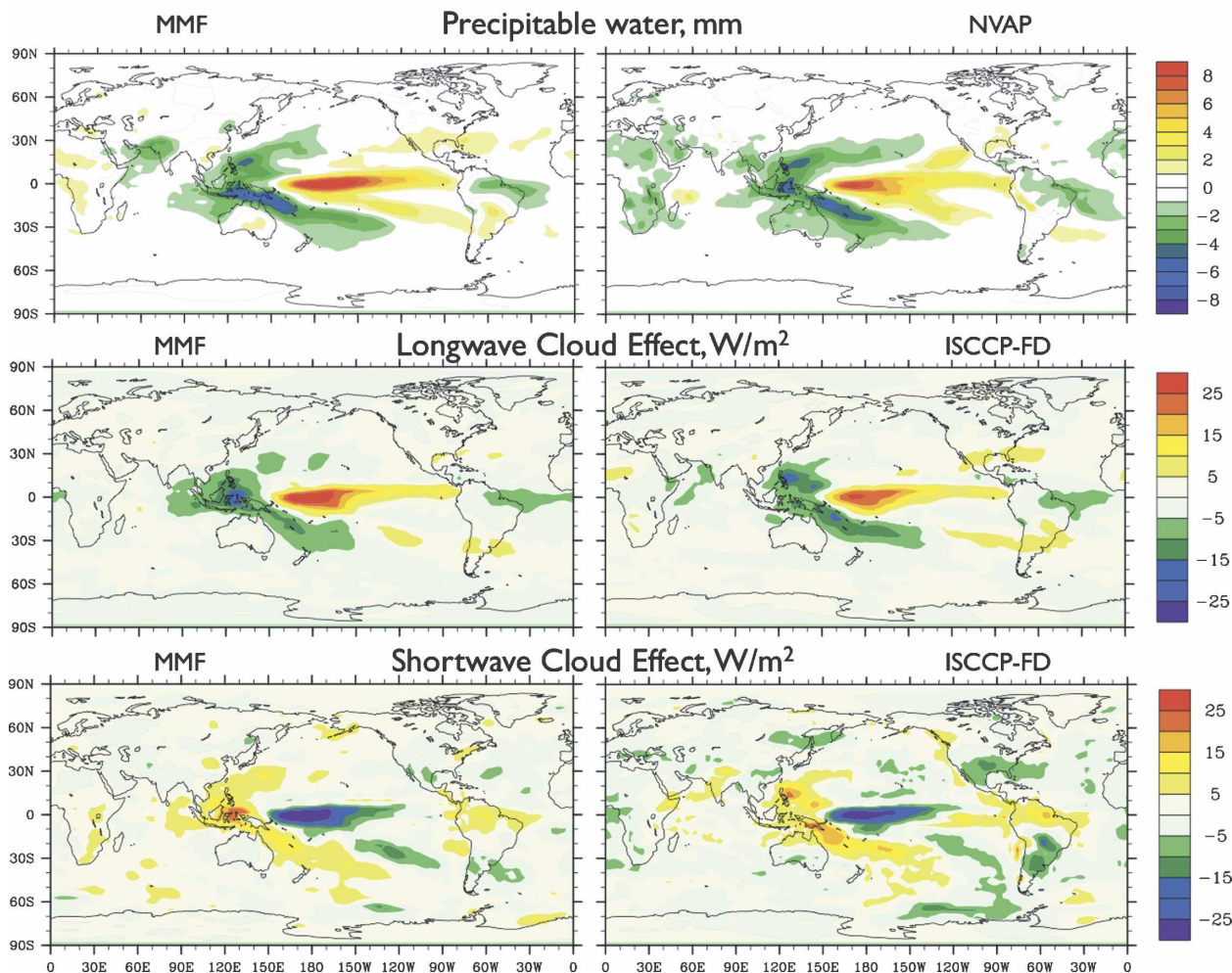## El Nino - La Nina Anomalies

FIG. 8. El Niño minus La Niña yearly anomaly composites of (top) precipitable water, (middle) longwave cloud effect, and (bottom) shortwave cloud effect (left) for the MMF simulation and (right) as observed.

lines in the figure are the theoretical dispersion curves for the shallow-water equations for selected equivalent depths. In the observations, the MJO occupies the spectral window of eastward wavenumbers 1–4 and periods greater than 30 days. The eastward-moving Kelvin waves and westward-moving Rossby waves follow the theoretical dispersion curves corresponding to a 25-m equivalent depth. In the MMF simulation, all three of these modes are captured quite well, especially in OLR. The Kelvin wave is a bit weak, but appears to propagate at about the observed speed. As in the observations, there is a clear frequency separation of the Kelvin wave from the MJO. In contrast, the simulation produced with the standard CAM3 lacks most of the MJO power with no clearly preferred wavenumber, and although the Kelvin wave has a strong amplitude, its phase speed

is too fast, corresponding to an equivalent depth of more than 50 m.

The same analysis for the zonal winds at 200 and 850 mb, respectively, is presented in Fig. 10. For the MMF and 40-yr European Centre for Medium-Range Weather Forecasts (ECMWF) Re-Analysis (ERA-40) results, MJO power is concentrated at zonal wavenumber 1, whereas the CAM evenly distributes its low-frequency power from wavenumbers −1 to +1, which is suggestive of a standing wave rather than a propagating one. The Kelvin wave is somewhat too fast in both simulations, but is otherwise well represented. At 850 mb, the wavenumber–frequency spectra for the MMF bears a strong resemblance to that of the ERA-40, characterized by a distinct spectral break between the MJO and slow-moving Kelvin waves. In the CAM, little
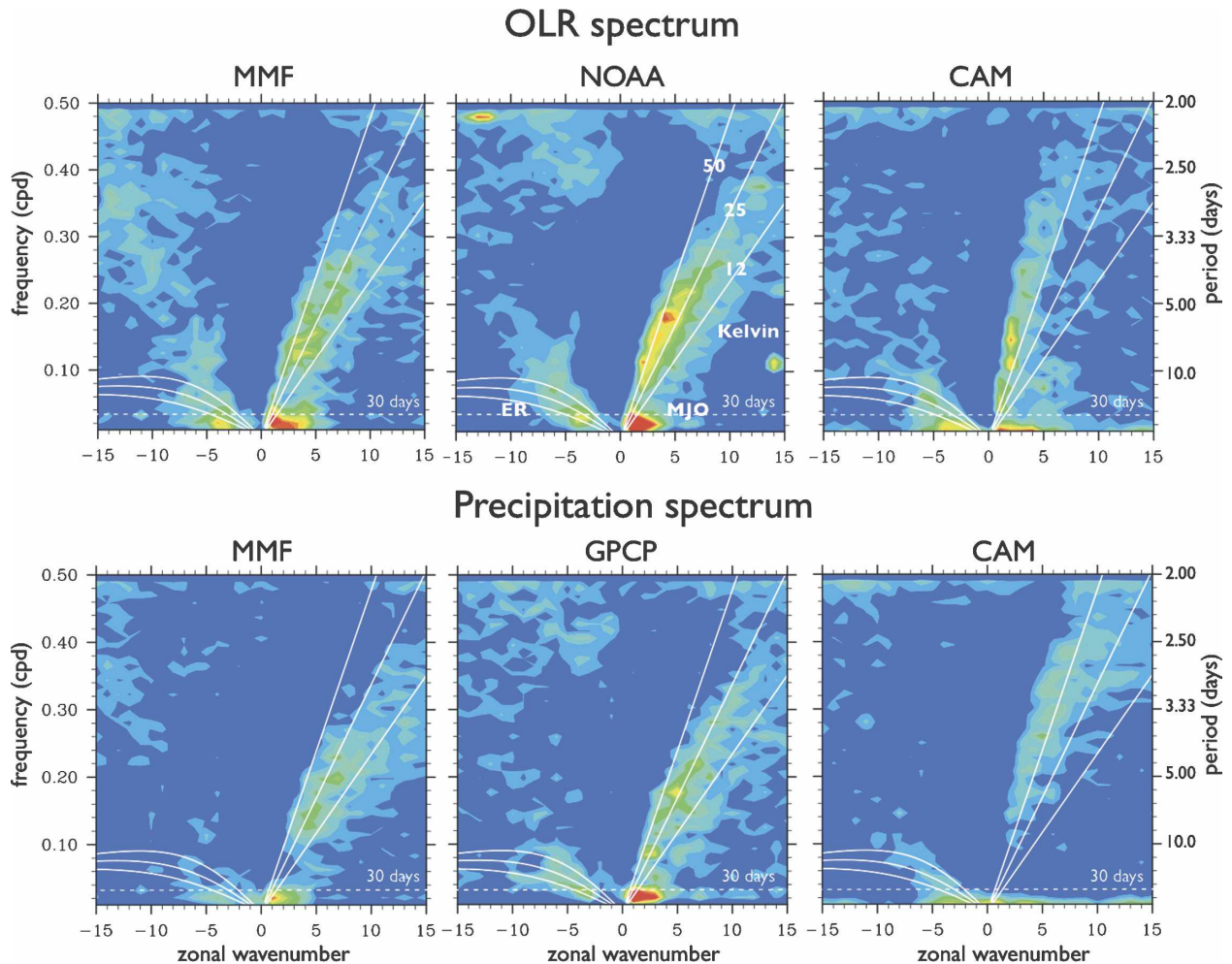
OLR spectrum

Precipitation spectrum

FIG. 9. The symmetric raw spectral power divided over the background power (signal-to-noise ratio spectrum) for the (top row) OLR and (bottom row) precipitation rate as (left) simulated by the MMF, (middle) derived from observations, and (right) simulated by the CAM3. Superimposed are the theoretical shallow-water dispersion curves for the equatorial Rossby and Kelvin waves for the equivalent depths of 12, 25, and 50 m. Contour interval is 0.1, with contours beginning at 1. Observations are 1979–2004 NOAA Advanced Very High Resolution Radiometer–interpolated OLR data (Liebmann and Smith 1996), and 1996–2005 daily GPCP data (Huffman et al. 2001).

power is seen in the MJO spectral space and the Kelvin wave is distinctly faster than that observed. The similarity in the shapes of these wavenumber–frequency plots to those seen for the observations and the MMF in Fig. 9 are evidence of strong convective coupling. Furthermore, the resemblance of the MMF precipitation spectrum to that of the Global Precipitation Climatology Project (GPCP) data indicates that MMF precipitation, and not just cloud fields, is organized on a large scale, similar to that found in nature.

The wavenumber–frequency spectra can be filtered to extract the signal associated only with particular disturbances of interest by zeroing the spectrum, except for the spectral region that contains the selected modes. The corresponding space–time structures of the se-

lected modes can then be generated from the filtered spectra using the inverse complex FFT.[2] The specific wavenumber–frequency windows used in the filtering procedure were the same as those used by WK99.

Figure 11 shows the geographical distribution for the simulated and observed OLR variance of the disturbances associated with the MJO averaged for the bo-

---

[2] Strictly speaking, the new dataset will also contain also some random noise contributed from the background spectrum at the same frequencies and wavenumbers as the desired disturbance. The amplitude of that noise will be much smaller than the amplitude of the disturbance though if the signal-to-noise ratio for that disturbance power spectrum is sufficiently larger than one, which is the case for the MJO, and Kelvin and Rossby waves.

200 hPa zonal wind spectrum
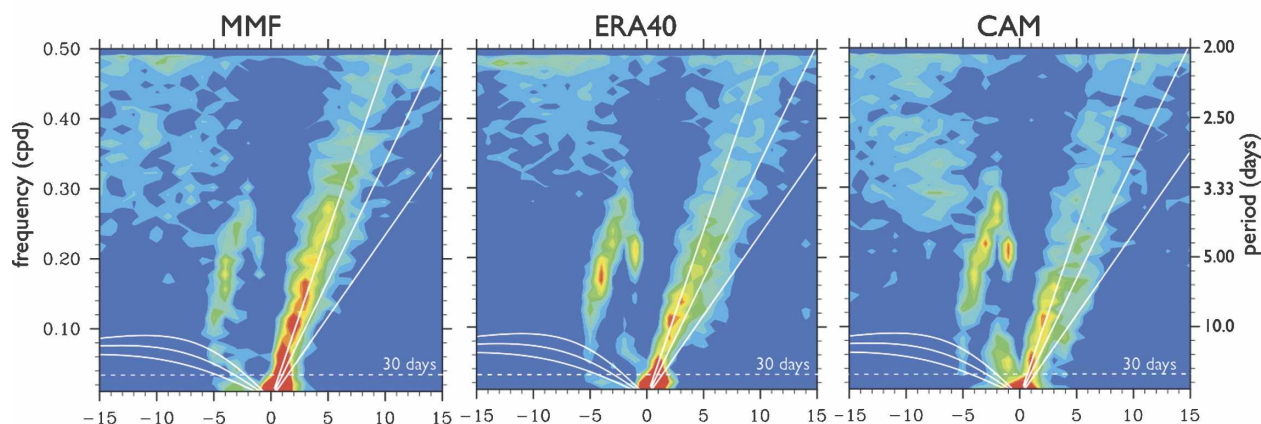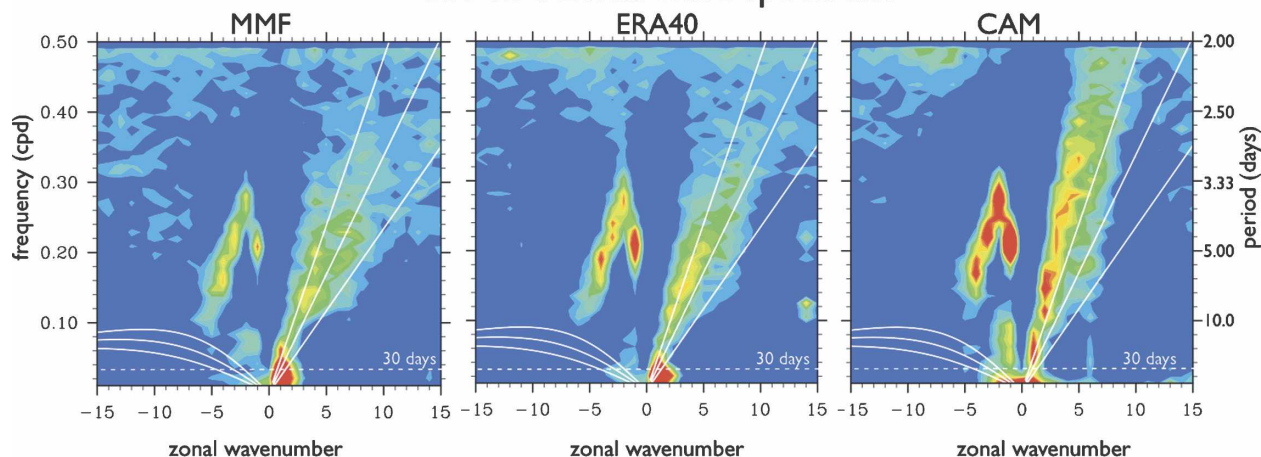

850 hPa zonal wind spectrum

FIG. 10. Similar to Fig. 9, but for the zonal component of wind at (top) 200 and (bottom) 850 mb. The observed daily wind is from the ERA-40 product.

real winter, boreal summer, and annual period. Overall, the pattern of OLR variability is well reproduced by the MMF. As in the observations, the simulated MJO is mostly confined to the Indian Ocean and the western Pacific. Also, the MJO is considerably stronger during the boreal winter, with the maximum activity just north from Australia, as observed. During boreal summer, the MJO can propagate much further eastward, just north from the equator, all the way to the Gulf of Mexico. This is also well captured by the MMF. However, the magnitude of the OLR variance is overestimated by about 50% (please note that different color bars are used for the MMF and observations). Unlike most of the GCMs, which typically produce an MJO that is too weak, the MMF tends to make the MJO stronger than that observed. As discussed by K05, experiments with convective momentum transport (using a version of the MMF that has a three-dimensional CRM) produce a slightly weaker, more realistic MJO.

Figure 12 compares the simulated and observed geographical distribution of variance associated with a Kelvin wave. As was the case with the MJO, the MMF does very good job in reproducing the Kelvin wave variance spatial pattern, as well as the seasonal variations; however, the magnitude of the variance is again overestimated.

To examine the seasonal and interannual variability of the MJO, one can plot the mean MJO-filtered OLR variance for each of the overlapping 96-day data segments against the time at the middle of the segment. This is shown in Fig. 13, along with the corresponding plot based on the National Oceanic and Atmospheric Administration (NOAA) OLR. Note that the multiyear mean variance was subtracted from both time series to accentuate the periods with below-average OLR anomalies, or weak MJO. In the MJO simulation, the periods with the strongest MJO events tend to occur during boreal winter, in agreement with observa-
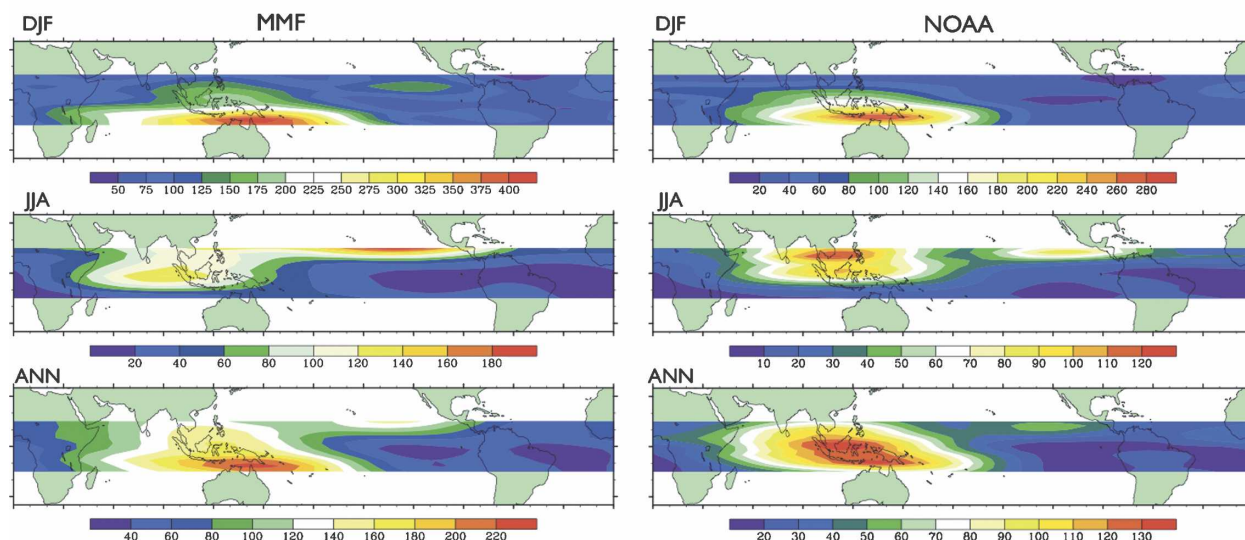
MJO-filtered variance

FIG. 11. The geographical distribution of the MJO-filtered OLR variance averaged for the (top) boreal winter, (middle) summer, and (bottom) annual mean for the (left) MMF simulation and (right) NOAA observations.

tions. The strength of the simulated MJO varies quite a bit from year to year. This is also seen in the observations.

4. MMF-specific analysis

The results described in section 3 are rather typical, in kind, of those seen in papers presenting GCM results. Because the MMF is still a GCM, it is important to present mean simulated climate and its variability in order to highlight the model's broad strengths and shortcomings. However, the MMF offers a wealth of additional information related to its ability to represent explicitly the cloud scales. This ability to take a close-up look at the cloud-scale processes and their interactions with the GCM grid-scale circulation constitutes a real advantage of the MMF over conventional GCMs. In this paper, only a few highlights are offered; a more
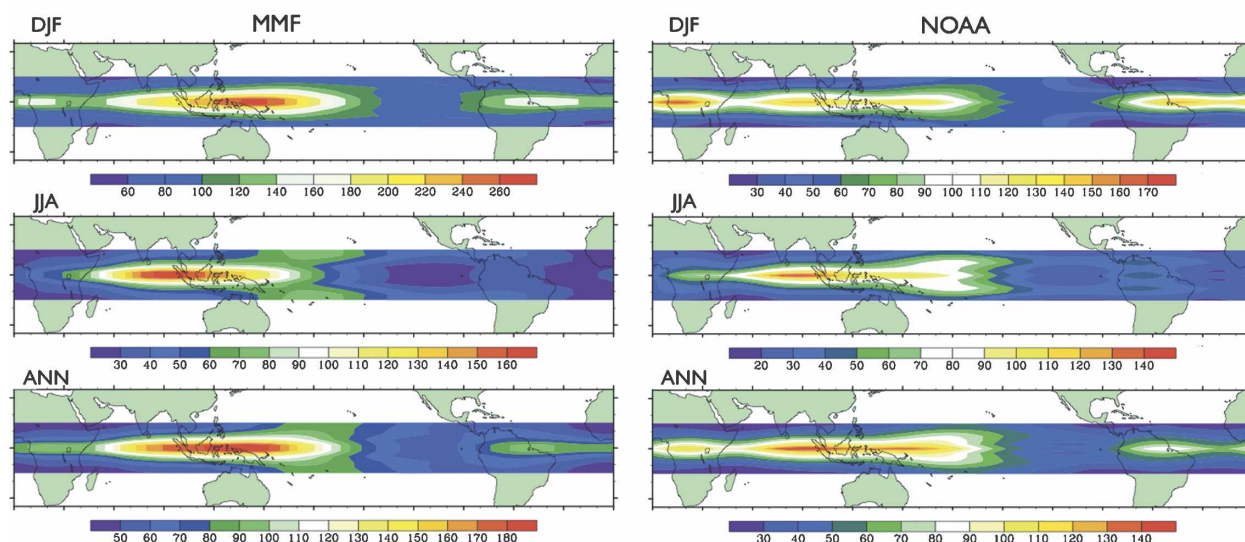
Kelvin-wave-filtered variance

FIG. 12. Same as Fig. 11, but for the Kelvin wave–filtered OLR anomaly.
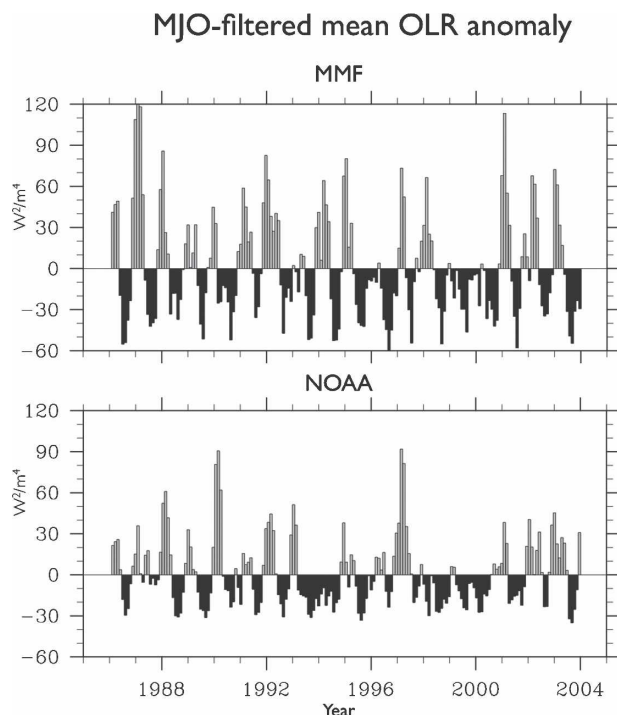
MJO-filtered mean OLR anomaly

FIG. 13. Time series of the 96-day-averaged MJO-filtered OLR variance for the (top) MMF simulation and (bottom) NOAA observations. The multiyear mean was removed.

comprehensive analysis of the cloud-scale statistics will be presented elsewhere.

Our analysis for this paper focuses on the Global Energy and Water Cycle Experiment (GEWEX) Cloud System Study (GCSS) Pacific cross section, which is a transect that spans northeast to southwest from just off the coast of southern California in North America, to the just south of the equator in the central Pacific Ocean. Cloud fields along this cross section are characterized by stratocumulus clouds at the northern limit, transitioning to broken shallow cumulus at the cross-sectional midpoint, and deep convection of the ITCZ at the southern limit. For this analysis, we saved 5 days of full-resolution (e.g., all thirty-two 4-km grid columns per GCM grid point) CRM output at hourly intervals from 1 to 5 July 1998.

The mean diurnal cycle of cloud water content, longwave (IR) cooling, vertical velocity variance, rainfall, and subcloud vertical velocity skewness for a stratocumulus section along the transect are shown in Fig. 14. Note that the cloud-scale w variance and skewness were computed from the CRM vertical velocity field. One can see that all fields exhibit a robust diurnal cycle: stratocumulus clouds are thick during the night and thin during the day. The temporal correlation between w variance, IR cooling, and negative skewness, which is

indicative of cloud-top cooling-induced downdrafts, all suggest that the CRM produces a cloud field, behaving in the manner consistent with our understanding of the stratocumulus-topped boundary layers, despite the relatively coarse grid spacing.

To look at the stratocumulus-to-cumulus transition zone, we used 1 month of 3-hourly output from July 1998 for the probability distribution function (PDF) of the pressure height of the temperature inversion at 20°N, 215°W along the Pacific cross section. Similar analysis was applied to the standard CAM output. Results from the two models are shown in Fig. 15. In the CAM, the temperature inversion pressure height peaks strongly at the ~840-mb level throughout the day, with little evidence of diurnal variability. In contrast, the MMF produces a broad distribution of the inversion height, with the deepest inversion layer found in the morning hours and the shallowest occurring in the late afternoon. This behavior of the inversion layer simulated by the MMF bears a remarkable resemblance to Fig. 14 of Miller et al. (1998), who computed the diurnal cycle of the transition zone heights from in situ observations in the Atlantic Ocean.

Another issue with the coarse grid resolution of the MMF's CRM is the possibility that the bulk of the vertical transport is produced by the parameterized SGS fluxes rather than by CRM-resolved or grid-scale circulations. The zonal mean cross sections of resolved and SGS fluxes of total nonprecipitating water shown in Fig. 16 demonstrate that, on average, the SGS fluxes account for less than 10% of the zonal mean total water fluxes, mostly in the boundary layer around the 975-mb model level. Locally at that pressure level, the SGS contribution can be larger as shown in Fig. 17. One can see that the contribution of SGS-parameterized fluxes does not generally exceed 30%; that is, in spite of the coarse spacing of the CRM grid used in the current version of MMF, the bulk of vertical transport of water in the MMF is carried out by the circulations explicitly represented on the CRM's grid. This is very encouraging.

5. Conclusions and future plans

An MMF is a climate model in which all of the conventional parameterizations of clouds and the boundary layer are replaced with a cloud-resolving model that explicitly represents the bulk of the dynamical processes that are unresolved by the GCM. The first 2-month integration using such a framework was presented in 2001. Since then, the results of a set of relatively short simulations have been reported in several publications that examined the aspects of mean sea-
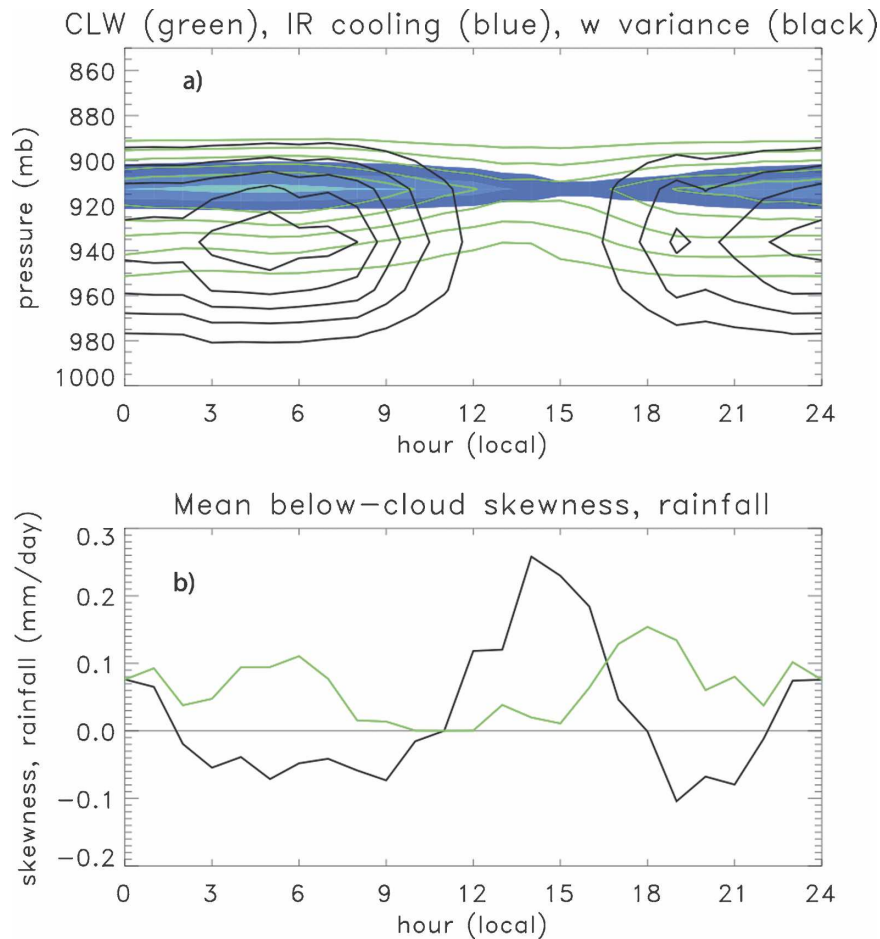
FIG. 14. Mean diurnal cycle of the stratus cloud field at 29°N, 227°W. (a) Cloud liquid water (green), longwave cooling (blue), and vertical velocity variance (black) are shown. Cloud liquid water contours are drawn every 0.1 g kg^{-1}. Longwave cooling is shaded for values greater than 15, 20, and 25 K day^{-1}. Vertical velocity variance contours are every 0.01 m^{-2} s^{-2}. (b) Rainfall (green) and normalized vertical velocity skewness averaged over the subcloud layer are also shown.

sonal climatology and subseasonal variability, climate sensitivity, the effects of radiation–cloud interactions, and domain dimensionality, among others. In this study, we present preliminary results from a 19-yr-long AMIP-style simulation in which the MMF is forced with prescribed SSTs and sea ice from September 1985 to September 2004. Such a prolonged simulation makes it possible to assess the ability of the MMF to simulate the interannual, seasonal, and subseasonal variability of the present climate. The observed changes in the atmospheric hydrological cycle and the TOA radiation fields, in response to the interannual variability of the SST, are generally well reproduced by the MMF, as is the seasonal cycle. The subseasonal variability associated with the MJO and the equatorially trapped waves is an area where MMF is particularly successful. An

area of concern is the overprediction by as much as 50% of the MJO-related variance of the outgoing longwave radiation. The seasonality of the MJO and its large interannual variability are quite realistically simulated by the MMF.

It is noteworthy, but beyond the scope of this paper, that despite the apparent success of MMF in reproducing many observed features of MJO, we still do not fully understand *why* the MMF climate simulations exhibit a robust MJO, while the simulations performed with the version of the same model using conventional parameterizations do not. In more general terms, is the MJO in the MMF reproduced the same way as in nature? What is important for the maintenance of the MJO? Grabowski and Moncrieff (2004), who used an idealized aquaplanet model and also a superparameteriza-
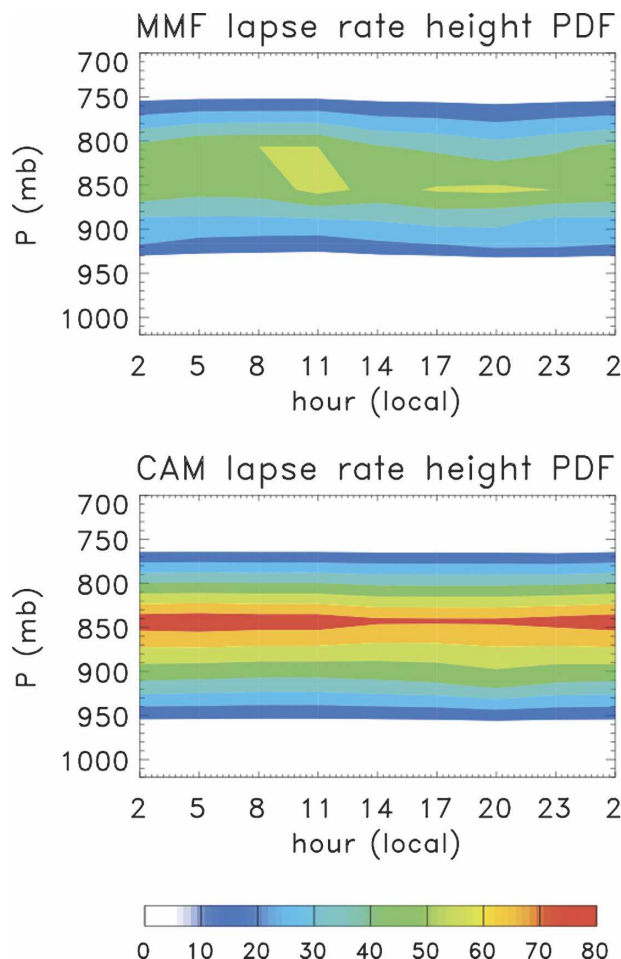
MMF lapse rate height PDF

CAM lapse rate height PDF

FIG. 15. Diurnal cycle of the PDF for the height of lapse rates exceeding 0 K km^{-1} in the Pacific cross section transition zone (20°N, 215°E). Contour interval is 10%.

tion of clouds, demonstrated that convective premoistening of the free troposphere is an important mechanism for maintenance of the MJO-like disturbances in their simulations. Is the ability of the cloud-resolving

model in the MMF to represent the details of interactions of clouds with the free troposphere what gives rise to a successful MJO simulation? These and many other questions can only be answered after further research.

Many aspects of the simulated mean multiyear climatology are quite familiar from our earlier experiments with prescribed climatological SST, such as persistent precipitation excesses in the Indian and Asian monsoon regions, large positive biases in the shortwave cloud effect resulting from a lack of stratocumulus and other low-level clouds, and an excessively cold tropical tropopause. Many of the biases associated with the hydrological cycle may be related to the parameterized microphysics in the cloud-resolving model, particularly the ice microphysics. Therefore, further refinement of the microphysics may lead to improvements in the performance of the model. The TOA flux biases associated with underprediction of the low-level clouds, including trade cumulus and stratocumulus clouds, are not as straightforward to alleviate. A simple increase of the grid resolution is currently not a viable option because it causes a dramatic increase in the already high computational cost of running MMF. Several possible pathways of addressing this problem without prohibitive cost increases are currently being tested.

Several results have been presented to demonstrate the physical realism of cloud fields that are simulated with the MMF, as well as the unique types of analyses that can be performed with this modeling approach. Examining cloud fields and processes on spatial scales comparable to the clouds themselves can reduce the need to deduce cloud field behavior based on parameterization assumptions. For the same reason, shortcomings in the MMF approach may be easier to identify than problems with traditional GCMs, which require interpreting model biases through the lens of parameterizations. Future MMF AMIP simulations will produce a larger set of CRM high-frequency data output at a variety of select locations, allowing further and more
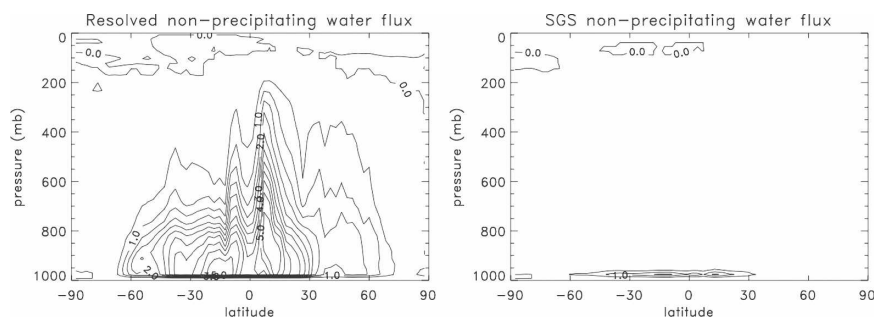

FIG. 16. Mean zonal MMF (left) resolved and (right) subgrid-scale fluxes of nonprecipitating water for 1–5 Jul 1998. Contour interval is 0.5×10^5 kg^{-1} m^{-2} s^{-1}.
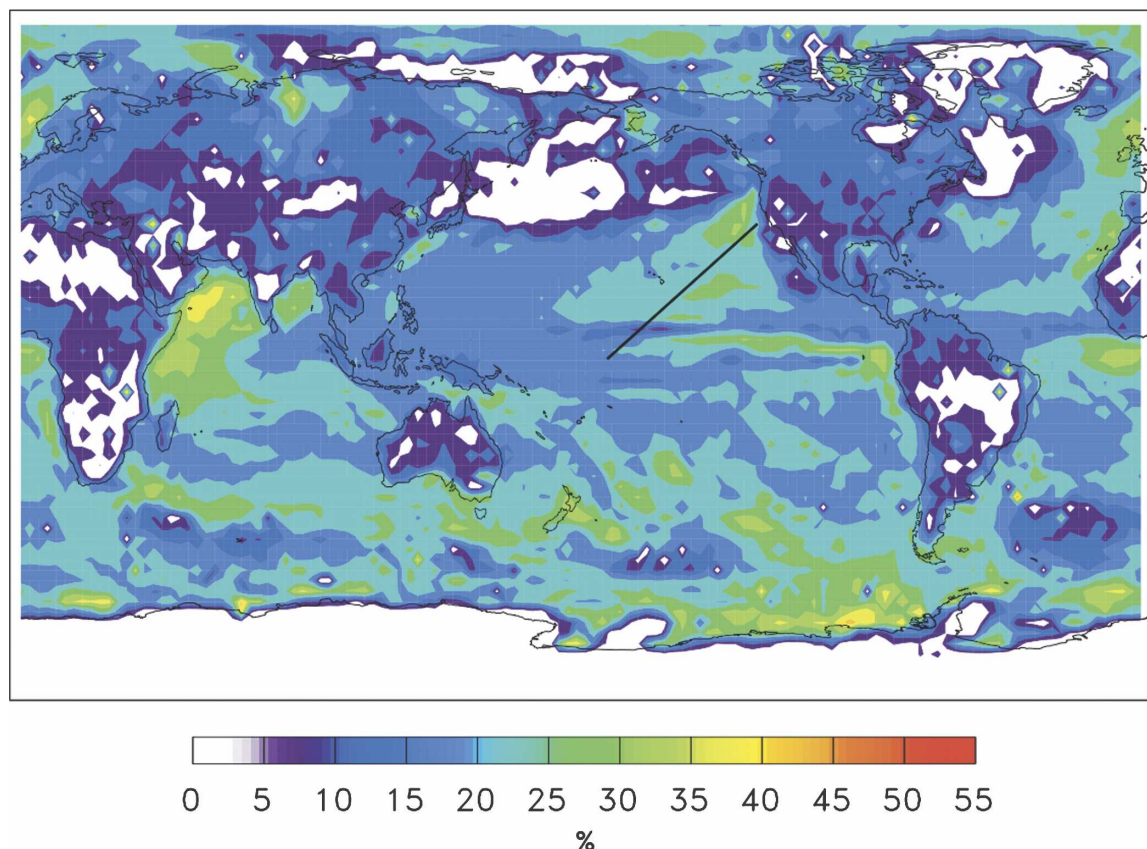
FIG. 17. A map of the time-averaged ratio of the SGS nonprecipitating water vapor fluxes to the total (resolved + SGS) fluxes computed by the MMF's CRM at the ~975-mb level for the 5-day period 1–5 Jul 1998. The Pacific cross section is shown as a black line going from the coast of California toward the equator.

detailed analyses of the cloud processes involved in ENSO and the MJO.

REFERENCES

Arakawa, A., 2004: The cumulus parameterization problem: Past, present, and future. *J. Climate,* **17,** 2493–2525.

Boville, B. A., P. J. Rasch, J. J. Hack, and J. R. McCaa, 2006: Representation of clouds and precipitation processes in the Community Atmosphere Model Version 3 (CAM3). *J. Climate,* **19,** 2184–2198.

Cess, R. D., and Coauthors, 1996: Cloud feedback in atmospheric general circulation models: An update. *J. Geophys. Res.,* **101,** 12 791–12 794.

Cole, J. N. S., H. W. Barker, D. A. Randall, M. F. Khairoutdinov, and E. E. Clothiaux, 2005: Global consequences of interac-tions between clouds and radiation at scales unresolved by global climate models. *Geophys. Res. Lett.,* **32,** L06703, doi:10.1029/2004GL020945.

Collins, W. D., P. J. Rasch, B. A. Boville, J. J. Hack, J. R. McCaa, D. L. Williamson, and B. P. Briegleb, 2006: The formulation and atmospheric simulation of the Community Atmosphere Model Version 3 (CAM3). *J. Climate,* **19,** 2144–2161.

Grabowski, W. W., 2001: Coupling cloud processes with the large-scale dynamics using the Cloud-Resolving Convection Parameterization (CRCP). *J. Atmos. Sci.,* **58,** 978–997.

——, and P. K. Smolarkiewicz, 1999: CRCP: A cloud resolving convective parameterization for modeling the tropical convective atmosphere. *Physica D,* **133,** 171–178.

——, and M. W. Moncrieff, 2004: Moisture-convection feedback in the tropics. *Quart. J. Roy. Meteor. Soc.,* **130,** 3081–3104.

Hack, J. H., J. M. Caron, S. G. Yeager, K. W. Oleson, M. M. Holland, J. E. Truesdale, and P. J. Rasch, 2006: Simulation of the global hydrological cycle in the CCSM Community Atmosphere Model Version 3 (CAM3): Mean features. *J. Climate,* **19,** 2199–2221.

Huffman, G. J., R. F. Adler, M. M. Morrissey, D. T. Bolvin, S. Curtis, R. Joyce, B. McGavock, and J. Susskind, 2001: Global precipitation at one-degree daily resolution from multisatellite observations. *J. Hydrometeor.,* **2,** 36–50.

Khairoutdinov, M. F., and D. A. Randall, 2001: A cloud resolving

model as a cloud parameterization in the NCAR Community Climate System Model: Preliminary results. *Geophys. Res. Lett.,* **28,** 3617–3620.

——, and ——, 2003: Cloud resolving modeling of the ARM summer 1997 IOP: Model formulation, results, uncertainties, and sensitivities. *J. Atmos. Sci.,* **60,** 607–625.

——, ——, and C. DeMotte, 2005: Simulations of the atmospheric general circulation using a cloud-resolving model as a superparameterization of physical processes. *J. Atmos. Sci.,* **62,** 2136–2154.

Kiehl, J. T., and K. E. Trenberth, 1997: Earth's annual global mean energy budget. *Bull. Amer. Meteor. Soc.,* **78,** 197–208.

King, M. D., and Coauthors, 2003: Cloud and aerosol properties, precipitable water, and profiles of temperature and water vapor from MODIS. *IEEE Trans. Geosci. Remote Sens.,* **41,** 442–458.

Klein, S., and C. Jacob, 1999: Validation and sensitivities of frontal clouds simulated by the ECMWF model. *Mon. Wea. Rev.,* **127,** 2514–2531.

Liebmann, B., and C. A. Smith, 1996: Description of a complete (interpolated) outgoing longwave radiation dataset. *Bull. Amer. Meteor. Soc.,* **77,** 1275–1277.

Lin, J.-L., and Coauthors, 2006: Tropical intraseasonal variability in 14 IPCC AR4 climate models. Part I: Convective signals. *J. Climate,* **19,** 2665–2690.

Madden, R. A., and P. R. Julian, 1972: Description of global-scale circulation cells in the tropics with a 40–50 day period. *J. Atmos. Sci.,* **29,** 1109–1123.

Miller, M. A., M. P. Jensen, and E. E. Clothiaux, 1998: Diurnal cloud and thermodynamic variations in the stratocumulus transition regime: A case study using in situ and remote sensors. *J. Atmos. Sci.,* **55,** 2294–2310.

Miura, H., H. Tomita, T. Nasuno, S. Iga, M. Satoh, and T. Matsuno, 2005: A climate sensitivity test using a global cloud resolving model under an aqua planet condition. *Geophys. Res. Lett.,* **32,** L19717, doi:10.1029/2005GL023672.

Ovtchinnikov, M., T. Ackerman, R. Marchand, and M. Khairoutdinov, 2006: Evaluation of the multiscale modeling framework using data from the Atmospheric Radiation Measurement Program. *J. Climate,* **19,** 1716–1729.

Randall, D. A., M. Khairoutdinov, A. Arakawa, and W. Grabowski, 2003: Breaking the cloud-parameterization deadlock. *Bull. Amer. Meteor. Soc.,* **84,** 1547–1564.

Randel, D. L., T. J. Greenwald, T. H. Vonder Haar, G. L. Stephens, M. A. Ringerud, and C. L. Combs, 1996: A new global water vapor dataset. *Bull. Amer. Meteor. Soc.,* **77,** 1233–1246.

Smagorinski, J., 1963: General circulation experiments with the primitive equations. I: The basic experiments. *Mon. Wea. Rev.,* **91,** 99–164.

Tomita, H., H. Miura, S. Iga, T. Nasuno, and M. Satoh, 2005: A global cloud-resolving simulation: Preliminary results from an aqua planet experiment. *Geophys. Res. Lett.,* **32,** L08805, doi:10.1029/2005GL022459.

Wheeler, M., and G. N. Kiladis, 1999: Convectively coupled equatorial waves: Analysis of clouds and temperature in the wavenumber-frequency domain. *J. Atmos. Sci.,* **56,** 374–399.

Wyant, M. C., M. Khairoutdinov, and C. S. Bretherton, 2006: Climate sensitivity and cloud response of a GCM with a superparameterization. *Geophys. Res. Lett.,* **33,** L06714, doi:10.1029/2005GL025464.

Xie, P., and P. A. Arkin, 1997: Global precipitation: A 17-year monthly analysis based on gauge observations, satellite estimates, and numerical model outputs. *Bull. Amer. Meteor. Soc.,* **78,** 2539–2558.

Zhang, Y. C., W. B. Rossow, A. A. Lacis, V. Oinas, and M. I. Mishchenko, 2004: Calculation of radiative fluxes from the surface to top of atmosphere based on ISCCP and other global data sets: Refinements of the radiative transfer model and the input data. *J. Geophys. Res.,* **109,** D19105, doi:10.1029/2003JD004457.